

PEGylated Superparamagnetic Iron Oxide Nanocrystal as MRI T₁-T₂ Dual-Modal Contrast Agent for Rat Liver Fibrosis Stage

Fulin Lu

North Sichuan Medical University

Liang Du

North Sichuan Medical University

Wei Chen

North Sichuan Medical University

Hai Jiang

North Sichuan Medical University

Chenwu Yang

North Sichuan Medical University

Yu Pu

North Sichuan Medical University

Jun Wu

North Sichuan Medical University

Jiang Zhu

North Sichuan Medical University

Tianwu Chen

North Sichuan Medical University

Xiaoming Zhang

North Sichuan Medical University

Changqiang Wu (✉ wucq1984@nsmc.edu.cn)

North Sichuan Medical University

Research Article

Keywords: Superparamagnetic iron oxide nanoparticles, Magnetic resonance imaging, Biliary liver fibrosis, Multimodal imaging, Medical image processing

Posted Date: April 6th, 2022

DOI: <https://doi.org/10.21203/rs.3.rs-1515292/v1>

License:  This work is licensed under a Creative Commons Attribution 4.0 International License.

[Read Full License](#)

Abstract

Background

The development of an effective method for staging liver fibrosis has always been a hot topic of research in the field of liver fibrosis diagnosis and therapy. T_1 - T_2 dual-modal contrast-enhanced MRI can provide complementary information with fault-free and self-confirm, and could be more objective and reliable for allowing quantitative evaluation of the liver parenchyma varieties at the progression of liver fibrosis.

Results

This study developed PEGylated small size superparamagnetic iron oxide nanocrystal (SPIO@PEG) for rat liver fibrosis magnetic resonance imaging (MRI) diagnosis and staging as a T_1 - T_2 dual-mode MRI contrast agent. SPIO@PEG was proved to have satisfactory biosafety and T_1 - T_2 dual-mode contrast effect under a 3.0 T MR scanner. In the following MR imaging of liver fibrosis rats in vivo, conventional T_1 and T_2 weighted imaging, T_1 and T_2 mapping of liver per- and post-intravenous administration of SPIO@PEG were systematically collected and analyzed. The results demonstrate that the combination of reduction rate of T_1 value ($\Delta T_1\%$) and T_2 value ($\Delta T_2\%$) could diagnose and distinguish the different stages of liver fibrosis. Furthermore, we creatively designed to fuse the T_1 and T_2 mapping images by Matrix laboratory (MATLAB) and quantitatively measured each rat's hepatic fibrosis positive pixel ratio (PPR). The results demonstrated that SPIO@PEG contrast-enhanced PPR could be used as a non-invasive biomarker to diagnose and discriminate the severity stages of biliary liver fibrosis.

Conclusion

The combination of T_1 - T_2 dual-modal contrast agent SPIO@PEG and MATLAB-based image fusion technology could be a promising method for diagnosing and staging liver fibrosis in the rat model.

Background

Nowadays, cholestatic liver fibrosis has quickly become one of the heated research hotspots with an increased relations to the mechanism of liver cirrhosis and liver failure associated with severe morbidity and mortality [1–4]. Moreover, some biliary liver fibrotic patients escaped the treatment and progressed toward liver cirrhosis or other end-stage liver diseases [5]. At present, the standard gold method for detecting and staging liver fibrosis in clinical practice is liver biopsy, which is limited by the intra-obvious bias, sampling error, and high cost [6]. Moreover, biopsy is an invasive method with infection risk and any other significant complications that are not suitable for dynamic observation and repeating examinations [7]. Traditional diffusion-weighted imaging (DWI) and ultrasound transient elastography are considered as two of the most potential diagnostic techniques for liver fibrosis [8]. Nevertheless, both two methods

have inherent drawbacks: the water molecules diffusion affection of DWI and the poor imaging quality of ultrasound transient elastography. Notably, both two methods are single-mode imaging techniques, their diagnosis and staging abilities could be significantly limited [9, 10]. For the above reasons, noninvasive multi-mode imaging techniques that can repeatedly evaluate liver fibrosis throughout the entire organ hold great promise for a more accurate assessment of fibrosis burden, progression, and treatment response is desperately needed on a clinical basis.

Great efforts have been made to develop a non-invasive and highly effective method for diagnosing and staging liver fibrosis. However, single-mode image modality provides limited information and cannot meet the requirements of complex disease diagnoses, surgery, and radiation therapy [11]. Among the existing techniques, magnetic resonance imaging (MRI) is considered to be a powerful multi-mode imaging technology, including T_1 mapping, T_2 mapping, magnetic resonance spectroscopy *et al.* and can be used to evaluate the patient from different aspects and make cross-validation for diseases [12, 13]. For example, the T_1 - T_2 dual-mode contrast-enhanced imaging can provide both T_1 and T_2 information to effortlessly distinguish the focal lesions from the normal tissue with fault-free and self-confirm MR images. The combination of T_1 and T_2 imaging modes might be a potential strategy since this method can make double-check of the obtained image data, yielding complementary information for sensitive and accurate MRI [14]. Furthermore, the measurement of T_1 and T_2 relaxation time by using T_1 and T_2 mapping may be more objective and reliable for qualifying quantitative evaluation of the relaxation time of liver parenchyma at the progression of liver fibrosis [15, 16].

Superparamagnetic iron oxide (SPIO) with good biosafety and low toxicity is commonly studied as a T_2 contrast agent for the liver. However, the negative contrast effect and low signal-to-noise ratio make it difficult to be widely applied in clinical [17]. Previous studies have demonstrated that the crystal size, surface coating, and aggregation state of SPIO are significantly related to its relaxivities (r_2 and r_1) and r_2/r_1 ratio [18, 19]. Moreover, we found that monodisperse small-size PEGylated SPIO nanocrystal (SPIO@PEG) has a high T_1 relaxivity and a modest r_2/r_1 ratio (< 10) at the magnetic field of 3.0T could be potentially used as a T_1 - T_2 dual-modal MR contrast agent [20]. That small-size MR nano-contrast agent combined the advantages of both T_1 and T_2 imaging modalities could be the key to being highly accurate and sensitive in the diagnosis and staging of liver fibrosis.

Herein, we creatively investigated the diagnosis and stage performance of SPIO@ PEG nanoparticles as a T_1 - T_2 dual-modal MR contrast agent of liver fibrosis under a clinical 3.0 T MR scanner. Based on the T_1 and T_2 mapping technology, we firstly fused the T_1 mapping and T_2 mapping images to verify the power of the double-checking process in the field of liver fibrosis in the rat model.

Results

Synthesis and Characterization of Small Size PEGylated Superparamagnetic Iron Oxide (SPIO@PEG).

Small size hydrophobic SPIO nanocrystals were synthesized by high-temperature thermal decomposition and were transferred to the aqueous phase by ligand exchange reaction (Fig. 2A). As shown in Fig. 2B, the SPIO nanocrystals have a small particle size (crystal size: 4 ± 0.15 nm in hexane and 5.21 ± 0.07 nm in water) in TEM and maintained good mono-dispersion before and after being transferred to the water phase. FTIR spectroscopy was used to characterize the surface coating of PEG. As shown in Fig. 2C, the band around $570\text{--}590\text{ cm}^{-1}$ was attributed to Fe-O stretching vibrations of the magnetite lattice. The presence of the peak at 1111 cm^{-1} was assigned to asymmetric and symmetric stretching vibrations of ACH_2 of PEG-DA. DLS was used to detect the particle size distribution of the SPIO nanocrystals in hexane and PEGylated SPIO in the aqueous solution (Fig. 2D). In solution, SPIO nanoparticles have a narrow particle size distribution, and the particle size is slightly increased after PEGylation (the number average size increase from 3.19 ± 1.13 nm to 6.86 ± 2.99 nm). All the results confirmed the successful preparation of small size SPIO@PEG nanoparticles.

Relaxivity of Small Size SPIO@PEG Nanoparticles.

To quantitatively evaluate the T_1 and T_2 dual-modal MRI contrast effect of the small size SPIO@PEG, the relaxivities (r_1 and r_2) of aqueous samples were measured at three main different magnetic fields (0.5, 1.5, and 3.0 T). As shown in Fig. 3A and Fig. 3B, the small size SPIO@PEG has high r_1 and r_2 simultaneously. However, r_1 decreases with the increase of magnetic field (from 0.5 to 3.0 T), while r_2 increases with the same magnetic field range, leading to the increase of the r_2/r_1 ratio. Significantly, the r_2/r_1 ratio of SPIO@PEG is 3.51 at 3.0 T, indicating that this SPIO@PEG is a T_1 - T_2 dual-modal contrast agent at 3.0 T (Fig. 3C). To further confirmation, FSE T_1 WI and T_2 WI of SPIO@PEG aqueous samples were carried out using a 3.0 T clinical MRI scanner to study the T_1 - T_2 dual-modal enhancement in vitro. As shown in Fig. 3D, the MRI signal intensity tends to be brighter with the increase of concentration in FSE T_1 WI. While in FSE T_2 WI, the signal intensity tends to be darker with the increase of Fe concentration. These results confirm that small size SPIO@PEG can be a proper T_1 - T_2 dual-modal contrast agent at 3.0 T MRI scanner.

Cytotoxicity Assay

The toxicity of SPIO@PEG was evaluated by the cell viability assay and the cytotoxicity was estimated using the Cell Counting Kit-8. SPIO@PEG nanoparticles do not show appreciable cytotoxicity at different drug loading concentrations, and there is no statistically significant difference ($P = 0.688$) compared with the blank group (without SPIO@PEG nanoparticles) shown in Fig. 3E. The result indicates that the small size SPIO@PEG has reliable biocompatibility.

Animal Model Establishment and Pathological Results.

A total of twenty-eight rats were enrolled in this study. Based on pathological findings, five rats were diagnosed with stage I of liver fibrosis (S1), five rats were diagnosed with stage II (S2), five rats were diagnosed with stage III (S3), and six rats were diagnosed with stage IV (S4). Seven normal rats were

comprised as the control group. Histologic analysis with HE staining and Masson's trichrome staining demonstrated uneven distributions of liver fibrosis in the experimental rats shown in Fig. 4.

In Vivo Contrast-Enhanced MRI of Liver Fibrosis in Rat Model.

To investigate the performance of SPIO@PEG in MRI enhancement of liver fibrosis stages. Axial T_1 and T_2 weighted imaging of rat livers were obtained under a 3.0 T MRI scanner before and after administration of the small size SPIO@PEG through the tail vein. Figure 5A shows the T_1 weighted MR imaging in different stages of liver fibrosis (S0 to S4). It is evident that the post enhanced images are brighter than the pre contrast enhanced images among all the groups. In contrast, for the T_2 weighted MR imaging, the post enhanced images are darker than the pre contrast enhanced images among the same groups (Fig. 5B). However, it has failed to discriminate the different stages of liver fibrosis from visual inspection. Subsequently, we measured the SNR and CNR of liver parenchyma and quantitatively analyzed the CNR changes of each rat in the two imaging modes ($\Delta\text{CNR-}T_1$, $\Delta\text{CNR-}T_2$). The results are shown in Fig. 5C and Fig. 5D. The $\Delta\text{CNR-}T_1$ gradually increased with the progression of liver fibrosis; on the contrary, the $\Delta\text{CNR-}T_2$ gradually decreased with the same range of liver fibrosis. Both these two parameters can be used to discriminate the non-fibrotic liver and stages ($S \geq 2$) of liver fibrosis. However, these two parameters are both challenging to distinguish adjacent stages of liver fibrosis.

In addition, the axial T_1 and T_2 mapping images were acquired, including pre- and post-injection of SPIO@PEG for all experimental rats. As Fig. 6A and Fig. 7A have depicted that all the T_1 and T_2 mapping images display regular changes with the progression of liver fibrosis, which can be supported by the increased T_1 and T_2 values shown in Fig. 6B and Fig. 7B. Post intravenous injection of SPIO@PEG, all the T_1 and T_2 values were decreased with different degrees (Fig. 6C and Fig. 7C). Moreover, both $\Delta T_1\%$ and $\Delta T_2\%$ were decreased with the range of fibrosis stages (S0 to S4). The image fusion procession result shows that after intravenous injection of SPIO@PEG the PPR gradually increases with the progression of liver fibrosis. The pre-contrasted enhanced PPR does not show any regular changes among different stages of liver fibrosis (Fig. 8C).

For statistical analysis, Spearman's correlation test depicts positive correlations between pre and post contrasted T_1 and T_2 values and liver fibrosis stages ($r = 0.867$ and 0.940 for T_1 value, $r = 0.608$ and 0.888 for T_2 value, respectively, $P < 0.001$). And PPR also shows positive correlations and liver fibrosis stages ($r = 0.979$, $P < 0.001$). In opposite, the $\Delta T_1\%$ and $\Delta T_2\%$ are negatively correlated to liver fibrosis stages ($r = -0.943$ and -0.784 , respectively, $P < 0.001$) (Table 1).

Table 1

The Spearman's rank correlation coefficient (r) and P value for the association between liver fibrosis stages and T_1 , T_2 values, as well as $T_1\%$ and $T_2\%$ obtained from pre- and post- SPIO@PEG contrast enhanced magnetic resonance images.

$\Delta\Delta$		
Parameter	r	P
$T_{1\text{pre}}$	0.876	< 0.001
$T_{1\text{post}}$	0.940	< 0.001
$\Delta T_1\%$	-0.943	< 0.001
$T_{1\text{pre}}$	0.608	< 0.001
$T_{2\text{post}}$	0.888	< 0.001
$\Delta T_2\%$	-0.784	< 0.001
PPR	0.979	< 0.001
Note: $\Delta T_1\% = [(T_{1\text{Pre}} - T_{1\text{Post}}) / T_{1\text{Pre}}] \times 100\%$, $\Delta T_2\% = [(T_{2\text{Pre}} - T_{2\text{Post}}) / T_{2\text{Pre}}] \times 100\%$, PPR = positive pixel ratio.		

Based on the Spearman's correlation test, the mean differences among different liver fibrosis subgroups were tested by one-way ANOVA. For the pre contrasted T_1 and T_2 parameters, there are significant differences between the control group (S0) and any other fibrotic groups. However, there are no statistical differences between the adjacent groups ($P < 0.05$), especially among S1, S2, and S3 subgroups (Fig. 6D and Fig. 7D). After intravenous administration of SPIO@PEG, the differences between the S2 and S3 are shown in post T_1 values and the S1 and S2 in post T_2 values. Nonetheless, single T_1 or T_2 parameters could not be able to discriminate the stage of liver fibrosis independently. Moreover, the $\Delta T_1\%$ and $\Delta T_2\%$ were also tested by one-way ANOVA. Interestingly, the $\Delta T_1\%$ differences between S0 and S1, S2 and S3, S3 and S4 were significantly different, but it was not significant between S1 and S2 stages (Fig. 6D). Notably, $\Delta T_2\%$ reached a statistically significant difference between the liver fibrosis groups of S1 and S2 ($P < 0.05$) (Fig. 7D). Nevertheless, these two parameters cannot independently distinguish the different stages of liver fibrosis. For PPR analysis, there is a significant difference among all the subgroups of liver fibrosis (Fig. 8C). Compared with the control group (S0), other groups exhibit higher PPR, which increases from 0.22 ± 0.04 to 0.89 ± 0.05 with the progression of liver fibrosis.

Repeatability and Reproducibility

The ICCs of the parameters including $\Delta\text{CNR-}T_1$, $\Delta\text{CNR-}T_2$, T_1 and T_2 pre and post contrasted were carried out between the two observers. All the parameters were shown good or excellent inter-observe agreement with repeatability and reproducibility. The $\Delta\text{CNR-}T_1$, $\Delta\text{CNR-}T_2$, pre- and post-contrast enhanced T_1 and T_2

relaxation times, and PPR with ICC values of 0.932, 0.943, 0.912, 0.923, 0.876, 0.897, and 0.927, respectively.

Distribution of Iron Nanoparticles

According to the Prussian blue stain pathological results, the liver specimen of the control group demonstrated that the deposition of iron nanoparticles is mainly distributed in the region of the portal track and its adjacent hepatic sinus. However, iron nanoparticles are mainly deposited along the edge fibrotic septa in fibrotic groups, and few iron nanoparticles can have the access to the fibrotic septa as shown in Fig. 9.

Discussion

The crucial element of liver fibrosis treatment efficiency relies on precise diagnosis and stage methods. T_1 - T_2 dual-modal small size SPIO@PEG enhanced MRI provides a non-invasive approach that combines both T_1 and T_2 contrast enhanced information may improve the diagnose and stage ability of liver fibrosis.

This present study confirmed a strong correlation between the relaxation times of the liver fibrosis stages. Additionally, the results showed that both T_1 and T_2 relaxation times were consistently elevated with the progression of hepatic fibrosis in rats. A number of human and animal studies have demonstrated that fibrosis could prolong the T_1 and T_2 relaxation times of the liver [21–23]. The prolonged T_1 and T_2 relaxation times were possibly caused by the pathophysiological alterations associated with activated liver fibrogenesis, characterized by inflammation, edema, and excess deposition of extracellular matrix (ECM) with the degree of fibrosis [24]. In histology, biliary liver fibrosis is characterized by chronic cholangitis and mainly affects septal and interlobular bile ducts [25]. Fibrogenesis in chronic cholestatic liver diseases could be seen as a classic chronic wound healing reaction that could directly activate fibrogenesis in liver parenchyma [26]. At early stages, liver parenchyma shows an intense inflammatory reaction. Moreover, the interlobular bile ducts are surrounded and infiltrated by immune/inflammatory cells causing structural damage and peribiliary stromal expansion, which could lead to a little higher T_1 value in S1 than S2 [27]. Then the portal venules are compressed and occluded by the inflammatory reaction. At later stages, the inflammation extends to the lobule, causing the formation of fibrous septa and collagenous fiber. The pattern of collagenous fiber accumulation can be characterized by an increased expression of several collagenous and non-collagenous extracellular matrix (ECM) components [28]. Collagen deposition could be the main significant influencing factor for the elevated unenhanced measurement of T_1 and T_2 values, as well as PPR. Unfortunately, our study revealed that liver parenchyma's unenhanced T_1 and T_2 relaxation times could not accurately differentiate the liver fibrosis stages.

After intravenous administration of small size SPIO@PEG nanoparticles, we found that both T_1 and T_2 values decreased with different degrees among different liver fibrosis stages. Our study firstly

demonstrated that the reduction rate of T_1 ($\Delta T_1\%$) and T_2 ($\Delta T_2\%$) both gradually decreased with the severity stages of biliary liver fibrosis (from S0 to S4) under T_1 - T_2 dual-modal small size SPIO@PEG enhanced MR images. Furthermore, the result reached significant differences between each set of adjacent hepatic fibrosis subgroups, providing potential biomarkers in precisely staging biliary liver fibrosis. However, these two parameters cannot independently distinguish the different fibrosis stages. Based on the study results of T_1 and T_2 values, we creatively fused the T_1 and T_2 mapping images and quantitatively measured the PPR of each rat. Compared with the control group (S0), other groups exhibited a higher PPR. Moreover, it reached significant differences among the different groups. These results collectively demonstrated the highly effective of T_1 - T_2 dual-mode SPIO@PEG diagnosis and stage ability of liver fibrosis.

According to the Prussian blue stain of the liver specimen after the administration of SPIO@PEG nanoparticles, we found that the iron particles mainly deposited along the edge of fibrotic septa in fibrotic rats. The deposition of collagen fibers takes up space of the perisinusoidal of Disse, leading to a variety of iron nanoparticle distribution among different fibrotic objects. The alteration of Iron nanoparticle distribution leads to the change of both MR signal intensity and relaxation times among different fibrosis stages [29]. In contrast, the deposition of iron particles in the healthy liver (S0) was randomly distributed in the hepatic sinus where HSCs most commonly reside. After administration of SPIO@PEG, on which the collagen deposition could not have an influence.

In this study, SPIO@PEG-enhanced T_1 -weighted MR imaging got higher ΔCNR with the range of fibrosis stages (S0 to S4), while the ΔCNR of T_2 got lower with the same range of fibrosis stages at 3.0T. Tanimoto A. [30] reported that patients with the chronic liver disease showed less signal intensity loss of background liver because of poor phagocytic activity of Kupffer cell dysfunction, and therefore, the cirrhotic liver is relatively superior compared with that of the non-cirrhotic liver. We believe that normal phagocytic function of Kupffer cells in the non-fibrotic liver can be attributed to the more significant signal intensity loss of liver parenchyma, and the incomplete phagocytic function of Kupffer cells in the fibrotic liver can be attributed to the improvement in the SNR of post-contrasted T_1 weight MR images, resulting in higher $\Delta\text{CNR}-T_1$. On the contrary, based on the blank hole effect of SPIO, the poor phagocytic activity of Kupffer cells in the fibrotic liver could result in a lower $\Delta\text{CNR}-T_2$ than non-fibrotic liver on T_2 weighted MR images at 3.0 T.

There are some advantages in our study. Firstly, T_1 - T_2 dual-modal magnetic resonance imaging combined with image fusion could avoid the false-positive signals caused by a single imaging mode and supply complementary and more accurate information for diagnosis and staging of diseases. Secondly, in order to remove the influence of liver steatosis and ensure the time resolution, we selected the LAVA sequence to access the T_1 and T_2 values. VFA T_1 mapping has been widely studied as a potential clinical application in detecting and diagnosing liver fibrosis [31]. VFA T_1 mapping was firstly introduced by Fram *et al.*, which is based on a series of T_1 -weighted spoiled gradient echo sequences with different flip angles [32]. At least two flip angles are required to calculate T_1 relaxation time. However, the method of

two flip angles could potentially decrease the accuracy and increase the estimation error of the T_1 value [33]. In this study, we used five flip angles to calculate the T_1 relaxation time, which could minimize the estimation error and increase the reliability of T_1 values. According to the study of Li J *et al.* [21] VFA T_1 mapping is a non-invasive, reliable, and accurate imaging method for assessing experimental liver fibrosis in rodents. Compared with ultrasound elastography, it provides similar good repeatability and reproducibility, a similar high accuracy for staging fibrosis, and a significantly better accuracy for detecting fibrosis regression. Thirdly, we used a 3.0 T scanner instead of a 1.5 T MR scanner for this study. The T_1 and T_2 values obtained with a 3.0T scanner can be more accurate than with a 1.5T scanner, which results in more reliable and accurate T_1 and T_2 values measurements in fibrotic or healthy livers.

Meanwhile, the combination of T_1 and T_2 mapping can integrate the high tissue resolution and high time resolution of T_1 mode contrast imaging and the high feasibility of soft tissue detection of T_2 mode contrast imaging.

Conclusion

In conclusion, we successfully synthesized T_1 - T_2 dual-modal small size SPIO@PEG nanoparticles, applied which to diagnose and discriminate the different stages of DDC-induced biliary liver fibrosis in the rat model. For the first time, we have demonstrated, that the PPR calculated by image fusion of T_1 and T_2 mapping could be used to discriminate different stages of biliary liver fibrosis. Furthermore, the PPR might be a noninvasive biomarker to distinguish the different stages of biliary liver fibrosis, which could be a promising non-invasive method to monitor the liver fibrosis progression and therapeutic response to the antifibrotic treatment.

Materials And Methods

Synthesis of Small-Size PEGylated Superparamagnetic Iron Oxide Nanocrystal (SPIO@PEG)

Small size SPIO@PEG were prepared as previously reported method [20] [34]. In brief, hydrophobic SPIO nanocrystals were synthesized by high-temperature thermal decomposition of iron acetylacetonate, and the small crystal size was composed by controlling the reaction heating conditions. After that, SPIO nanocrystals were transferred to aqueous phase by ligand exchange reaction with the sodium citrate. Subsequently, PEG-DA was coated on the surface of SPIO nanocrystals in an aqueous environment. The crystal size and dispersity were examined using transmission electron microscopy (TEM) and dynamic light scattering (DLS). The composition changes of SPIO nanocrystals were characterized by Fourier transform infrared spectroscopy (FTIR). The concentration of iron was determined by using an atomic absorption spectrometer (AAS).

In Vitro MRI Study of Small-Size SPIO@PEG Nanoparticles

Small-size SPIO@PEG aqueous samples with different iron concentrations (0.1, 0.2, 0.3, 0.4, and 0.5 mmol/L) were prepared and placed in 2 mL test bottles. Longitudinal and transverse relaxation times (T_1 and T_2) were measured at room temperature at 0.5 T (Magnetic resonance developer relaxation rate analyzer, Niumag, Shanghai, China), 1.5 T (Minispec Mq60 NMR Analyzer, Bruker, Beijing, China), and 3.0 T (Discovery MR750, GE Medical System, Milwaukee, WI), respectively. Then, the T_1 and T_2 relaxivities ($1/T_1$ and $1/T_2$, s^{-1}) were determined by curve fitting of the longitudinal or transverse relaxation rate (r_1 or r_2 , s^{-1}) versus of the Fe concentration. MR imaging of samples was performed under a clinical 3.0 T MR scanner (Discovery MR750, GE Medical System, Milwaukee, WI) with a head coil. Axial images of the phantoms were acquired by T_1 -weighted spin-echo sequence (repetition time = 200 ms, echo time = 9 ms, matrix = 320×320 , field of vision = 18×18 mm, slice thickness = 3 mm, flip angle = 90°) and T_2 weighted spin echo sequence (repetition time = 2500 ms, echo time = 100 ms, matrix = 320×320 , field of vision = 18×18 mm, slice thickness = 3 mm, flip angle = 90°).

Cytotoxicity Assay.

SPIO@PEG nanoparticles were tested for cytotoxicity on hepatic cancer cells (Hep G2). Hep G2 was provided by the Chinese Academy of Sciences Cell Bank (Shanghai, China). The cells were cultured in Dulbecco's modified Eagle's medium (DMEM)/high glucose (4.5 g/L glucose) containing 10% (v/v) fetal bovine serum (Biological Industries, Israel) and 1% (v/v) penicillin-streptomycin (Hyclone, Logan, UT) at 37°C , 5% CO_2 , and saturated humidity. Hep G2 cells were plated in 96-well plates at 4×10^3 cells per well (100 μL) of complete media. The cells were added with varying concentrations (5, 10, 15, and 20 $\mu\text{g}/\text{ml}$) of SPIO@PEG nanoparticles and with a followed incubation for 24 h. Afterward, each well was added with a 10 μL Cell Counting Kit-8 (CCK-8) solution (Boster Biological Technology, Wuhan, China) and incubated at 37°C for 1 h in the following. The absorbance of the samples was measured using a microplate reader (Thermo Scientific). Cell viability was calculated according to the equation: Cell viability (%) = $(N_S / N_C) \times 100\%$, where N_S and N_C are the absorbances of living cells treated with or without SPIO@PEG nanoparticles. And the absorbance measurements were used and corrected as blank control group.

Animal Liver Fibrosis Model

This study has been approved by the Ethics Committee of our research institution (NSMC-2021-79). All experimental procedures were followed in strict accordance with the proposal in the Guide for the Care and Use of Laboratory Animals of the National Institutes of Health. Healthy male Sprague-Dawley (SD) rats (180-200g and 6–7 weeks old) were obtained from the Experimental Animal Center of our institute. Twenty-eight rats were randomly divided into the control group and four experimental groups. The control group rats ($n = 7$) were fed a standard commercial diet. The four experimental groups were fed a 0.1% 3,5-diethoxycarbonyl-1,4-dihydro-collidine (DDC) supplemented diet (Tokyo Chemical Industry, Co, LTD, Tokyo, Japan) for 1 week, 4 weeks, 8 weeks and 12 weeks, respectively, to build different stages of biliary liver fibrotic model [35]. All animals were raised at $23 \pm 3^\circ\text{C}$ with a 12:12h light/dark cycle and tap water ad libitum.

In Vivo MR Imaging

All MR imaging was performed at a 3.0 T MRI scanner (GE healthcare, MR750 Medical System, Milwaukee, WI). The rats were inhaled anesthetized by isoflurane (RWD Life Science, Shenzhen, China) with a face mask (Anesthetic Conc.: 1.0-1.5%; 20–30 mL O₂/kg) and transferred to the MR scanner. A custom-made animal receiver coil was used to obtain the MR images. MRI scans were carried out before (pre) and immediately after (post) SPIO@PEG intravenous injection at a dose of 2.5 mg (Fe) /kg body weight through the tail vein of the rats. Conventional T_1 and T_2 weighted MR imaging were also performed pre- and post-contrast injection, and the detail parameter of T_1 and T_2 -weighted sequences were as follows: T_1 weighted imaging (GRE sequence, repetition time (TR) = 9 ms, echo time (TE) = 3 ms, flip angle (FA) = 30°, field of view (FOV) = 80 × 80 mm); T_2 weighted imaging (fast spin-echo sequence, TR = 4000 ms, TE = 76 ms, FA = 90°), FOV = 80 × 80 mm and slice thickness = 2.0 mm).

T_1 mapping images were acquired by using the variable flip angle (VFA) technique [36] which contains a series of rat liver acquisition volume acceleration (LAVA) with five different flip angles (3, 6, 9, 12, and 15°). The followings are the MR imaging parameters: TR = 5.0 ms, TE = 2.4 ms, number of excitations = 4, FOV = 80 × 80 mm, matrix = 512 × 512, reconstruction matrix = 400 × 400, bandwidth = 83.33 Hz per pixel, slice thickness = 0.8 mm. T_2 mapping images were acquired by using free-breath fast spin echo (FES) sequences, the detail parameters were as follows: TR = 1200 ms, TE = 8, 16, 24, 32, 40, 48, 56, and 64 ms, number of excitations = 2, FA = 90°, FOV = 80 × 80 mm, matrix = 512 × 512, reconstruction matrix = 400 × 400, bandwidth = 166.67 Hz per pixel, thickness = 2.0 mm, slice space = 0.6 mm.

Image Analysis

Two experienced radiologists performed image analyses with three and fourteen diagnosis experiences who were blinded to both the animal groups and pathologic results of this study. The conventional T_1 and T_2 weighted MR images, including pre- and post-contrasted images, were presented on a picture archiving and communication system (PACS; GE Advantage Workstation Version 4.4-09, Sun Microsystems, Palo Alto, CA, USA) with an optimal window setting adjustment. Subsequently, we measured each experimental rat's signal to noise ratios (SNR = *mean signal intensity of the liver / background noise*). Furthermore, based on the SNR measurements, the contrast-to-noise ratio ($\Delta\text{CNR} = \text{abs}(SNR_{pre} - SNR_{post})$) as described by Siedek F *et al.* [37] was calculated for each rat include T_1 and T_2 weighted MR images pre and post SPIO@PEG enhanced ($\Delta\text{CNR-}T_1$ and $\Delta\text{CNR-}T_2$, respectively).

T_1 mapping and T_2 mapping images, including pre- and post-contrasted images, were transferred to matrix laboratory (MATLAB) for the next analysis. T_1 relaxation times were measured by the VFA method, which has been demonstrated by Deoni SC *et al.* [36]. Three regions of interest (ROIs) of one section were respectively drawn within the liver parenchyma and constantly measured on five liver sections of each rat, avoiding confounding factors like biliary structures, vessels, and organ boundaries. The size of ROI was controlled within 0.8-1.2cm². The ROIs were first placed into the pre-contrast T_1 and T_2 mapping. And

then, the ROIs were copied and placed on the same area on post-contrast relaxation maps for each rat. Mean T_1 and T_2 values were used for further analyses. The decreasing rate of T_1 relaxation time ($\Delta T_1\%$) and T_2 relaxation time ($\Delta T_2\%$) were calculated as $\Delta T_1\% = (T_{1\text{pre}} - T_{1\text{post}}) / T_{1\text{pre}} \times 100\%$ and $\Delta T_2\% = (T_{2\text{pre}} - T_{2\text{post}}) / T_{2\text{pre}} \times 100\%$. Where $T_{1\text{pre}}$ (or $T_{2\text{pre}}$) and $T_{1\text{post}}$ (or $T_{2\text{post}}$) are relaxation times of pre- and post- the small size SPIO@PEG injection via the tail vein of rat [38].

Based on the calculated relaxation time of T_1 and T_2 , we adapted the T_1 mapping and T_2 mapping sequences for the T_1 - T_2 dual-mode image fusion. Firstly, we associated the T_1 mapping and T_2 mapping images with image registration. Secondly, the pixel of ROIs in these two sequences was dividing and coloring via a "logic gate". The logic gate was briefly depicted in Fig. 8. Third, the number of positive pixels and all the pixels in ROIs were measured to calculate the PPR (PPR = *the number of positive pixel / all the pixel in ROI*). It is worth noting that, the threshold value of the logic gate was defined as subtracting the mean reduction value of T_1 and T_2 values from corresponding pre-contrasted enhanced T_1 and T_2 values. All the image fusion analyses were performed by using MATLAB (version 9.7 (R2019b), Mathworks, USA).

Statistical Analysis

All the quantitative data were shown as mean \pm standard deviation. All the statistical analyses were performed by using commercial software SPSS (SPSS version 26.0, SPSS Inc., Chicago, IL). Spearman's ranked correlation test was used to investigate the correlation between the ΔCNR ($\Delta\text{CNR-}T_1$ and $\Delta\text{CNR-}T_2$), relaxation time parameters (T_1 values, T_2 values, $\Delta T_1\%$, and $\Delta T_2\%$), PPR, and pathological liver fibrosis stages. Unpaired student's *t*-test or one-way analysis of variance (ANOVA) were used to compare the mean-variance between different fibrosis groups. Intraclass correlation coefficient (ICC) was used to test the consistency of signal intensity and relaxation time measurements of two observers, ICC values less than 0.5, between 0.5 and 0.75, between 0.75 and 0.90, and greater than 0.90 represent poor, moderate, good, and excellent repeatability, respectively [39]. All tests were two-tail with a *P* value less than 0.05 was considered statistically significant.

Histopathological Analysis

After MRI examination, animals were sacrificed by cervical dislocation under deep anesthesia with isoflurane, and the livers were removed and immediately fixed in 10% formalin. All the liver samples were stained with hematoxylin-eosin stain (HE), Masson's trichrome stain, and Prussian blue stain. Pathologic analysis was regarded as the reference standard of staging rat liver fibrosis according to the METAVIR classification score system [40], in which S0 = no fibrosis, S1 = portal fibrosis without septa, S2 = portal fibrosis and a few septa, S3 = numerous septa without cirrhosis, and S4 = cirrhosis. A pathologist with five years' experience in the diagnosis of liver pathology, has evaluated the stage of liver fibrosis (S0-S4) based on the standard classification mentioned before.

Abbreviations

PEG
Polyethylene glycol
SPIO@PEG
PEGylated superparamagnetic iron oxide nanocrystal MRI:Magnetic resonance imaging
 $\Delta T_1\%$
Reduction rate of T_1 value
 $\Delta T_2\%$
Reduction rate of T_2 value
MATLAB
Matrix laboratory
PPR
Positive pixel ratio
SNR
Signal to noise ratio
CNR
Contrast to noise ratio
LAVA
Liver acquisition volume acceleration
VFA
Variable flip angle
DDC
3,5-diethoxycarbonyl-1,4-dihydro-collidine
TEM
Transmission electron microscopy
DLS
Dynamic light scattering
FTIR
Fourier transform infrared spectroscopy
AAS
Atomic absorption spectrometer
GRE
Gradient recalled echo
FSE
Fast spin echo
TR
Repetition time
TE
Echo time
FA
Flip angle

FOV
Field of view
ROI
Region of interest
ICC
Intraclass correlation coefficient
One-way ANOVA
One-way analysis of variance.

Declarations

Ethics approval and consent to participate

This study has been approved by the Ethics Committee of our research institution (NSMC-2021-79). All experimental procedures were followed in strict accordance with the proposal in the Guide for the Care and Use of Laboratory Animals of the National Institutes of Health.

Consent for publication

All authors consent for publication.

Availability of data and materials

All data generated or analyzed during this study are included in this published article.

Competing interests

The authors report no conflicts of interest in this work.

Funding

The work was supported by National Natural Science Foundation of China (81601490), Science and Technology Project of Municipal School Strategic Cooperation, Nanchong (20SXQT0306), Pre-research Project of North Sichuan Medical College (CBY19-YZ05), Open Research Program of Antibiotic Research and Reevaluation Key Laboratory of Sichuan Province (ARRLKF20-03).

Acknowledgements

Not applicable.

Author details

1. Medical Imaging Key Laboratory of Sichuan Province and School of Medical Imaging, Affiliated Hospital of North Sichuan Medical College, Nanchong, 637000, People's Republic of China.

References

1. Bataller R, Brenner DA: **Liver fibrosis**. *J Clin Invest* 2005, **115**:209–218.
2. Pinzani M, Rosselli M, Zuckermann M: **Liver cirrhosis**. *Best Pract Res Clin Gastroenterol* 2011, **25**:281–290.
3. Ortiz-Perez A, Donnelly B, Temple H, Tiao G, Bansal R, Mohanty SK: **Innate Immunity and Pathogenesis of Biliary Atresia**. *Front Immunol* 2020, **11**:329.
4. Sakiani S, Kleiner DE, Heller T, Koh C: **Hepatic Manifestations of Cystic Fibrosis**. *Clin Liver Dis* 2019, **23**:263–277.
5. Corpechot C, Carrat F, Poupon R, Poupon RE: **Primary biliary cirrhosis: incidence and predictive factors of cirrhosis development in ursodiol-treated patients**. *Gastroenterology* 2002, **122**:652–658.
6. Castera L: **Assessing liver fibrosis**. *Expert Rev Gastroenterol Hepatol* 2008, **2**:541–552.
7. Germani G, Hytiroglou P, Fotiadu A, Burroughs AK, Dhillon AP: **Assessment of fibrosis and cirrhosis in liver biopsies: an update**. *Semin Liver Dis* 2011, **31**:82–90.
8. Tien PC, Duarte M, Roque A, Price J: **MRE and ELF in Liver Fibrosis Assessment: Are Two Better Than One?** *Dig Dis Sci* 2020, **65**:928–930.
9. Sharma S, Khalili K, Nguyen GC: **Non-invasive diagnosis of advanced fibrosis and cirrhosis**. *World J Gastroenterol* 2014, **20**:16820–16830.
10. Agbim U, Asrani SK: **Non-invasive assessment of liver fibrosis and prognosis: an update on serum and elastography markers**. *Expert Rev Gastroenterol Hepatol* 2019, **13**:361–374.
11. Yang Y, Wu J, Huang S, Fang Y, Lin P, Que Y: **Multimodal Medical Image Fusion Based on Fuzzy Discrimination With Structural Patch Decomposition**. *IEEE J Biomed Health Inform* 2019, **23**:1647–1660.
12. Zhao R, Hamilton G, Brittain JH, Reeder SB, Hernando D: **Design and evaluation of quantitative MRI phantoms to mimic the simultaneous presence of fat, iron, and fibrosis in the liver**. *Magn Reson Med* 2021, **85**:734–747.
13. Zhao R, Hernando D, Harris DT, Hinshaw LA, Li K, Ananthakrishnan L, Bashir MR, Duan X, Ghasabeh MA, Kamel IR, et al: **Multisite multivendor validation of a quantitative MRI and CT compatible fat phantom**. *Med Phys* 2021, **48**:4375–4386.
14. Wang J, Jia Y, Wang Q, Liang Z, Han G, Wang Z, Lee J, Zhao M, Li F, Bai R, Ling D: **An Ultrahigh-Field-Tailored T1 -T2 Dual-Mode MRI Contrast Agent for High-Performance Vascular Imaging**. *Adv Mater* 2021, **33**:e2004917.
15. Long MT, Benjamin EJ: **Prevalent Cardiovascular Disease Events and T1 Mapping Defined Hepatic Fibrosis**. *Circ Cardiovasc Imaging* 2018, **11**:e007553.
16. Pan S, Wang XQ, Guo QY: **Quantitative assessment of hepatic fibrosis in chronic hepatitis B and C: T1 mapping on Gd-EOB-DTPA-enhanced liver magnetic resonance imaging**. *World J Gastroenterol* 2018, **24**:2024–2035.

17. Xiao YD, Paudel R, Liu J, Ma C, Zhang ZS, Zhou SK: **MRI contrast agents: Classification and application (Review)**. *Int J Mol Med* 2016, **38**:1319–1326.
18. Xie W, Guo Z, Gao F, Gao Q, Wang D, Liaw BS, Cai Q, Sun X, Wang X, Zhao L: **Shape-, size- and structure-controlled synthesis and biocompatibility of iron oxide nanoparticles for magnetic theranostics**. *Theranostics* 2018, **8**:3284–3307.
19. Doig M, Warrens CP, Camp PJ: **Structure and friction of stearic acid and oleic acid films adsorbed on iron oxide surfaces in squalane**. *Langmuir* 2014, **30**:186–195.
20. Deng LH, Jiang H, Lu FL, Wang HW, Pu Y, Wu CQ, Tang HJ, Xu Y, Chen TW, Zhu J, et al: **Size and PEG Length-Controlled PEGylated Monocrystalline Superparamagnetic Iron Oxide Nanocomposite for MRI Contrast Agent**. *Int J Nanomedicine* 2021, **16**:201–211.
21. Li J, Liu H, Zhang C, Yang S, Wang Y, Chen W, Li X, Wang D: **Native T1 mapping compared to ultrasound elastography for staging and monitoring liver fibrosis: an animal study of repeatability, reproducibility, and accuracy**. *Eur Radiol* 2020, **30**:337–345.
22. Luetkens JA, Klein S, Traber F, Schmeel FC, Sprinkart AM, Kuetting DLR, Block W, Uschner FE, Schierwagen R, Hittatiya K, et al: **Quantification of Liver Fibrosis at T1 and T2 Mapping with Extracellular Volume Fraction MRI: Preclinical Results**. *Radiology* 2018, **288**:748–754.
23. Chow AM, Gao DS, Fan SJ, Qiao Z, Lee FY, Yang J, Man K, Wu EX: **Measurement of liver T(1) and T(2) relaxation times in an experimental mouse model of liver fibrosis**. *J Magn Reson Imaging* 2012, **36**:152–158.
24. Hoffman DH, Ayoola A, Nickel D, Han F, Chandarana H, Shanbhogue KP: **T1 mapping, T2 mapping and MR elastography of the liver for detection and staging of liver fibrosis**. *Abdom Radiol (NY)* 2020, **45**:692–700.
25. Pinzani M, Luong TV: **Pathogenesis of biliary fibrosis**. *Biochim Biophys Acta Mol Basis Dis* 2018, **1864**:1279–1283.
26. Ghonem NS, Assis DN, Boyer JL: **Fibrates and cholestasis**. *Hepatology* 2015, **62**:635–643.
27. Gulamhusein AF, Hirschfield GM: **Primary biliary cholangitis: pathogenesis and therapeutic opportunities**. *Nat Rev Gastroenterol Hepatol* 2020, **17**:93–110.
28. Lleo A, Marzorati S, Anaya JM, Gershwin ME: **Primary biliary cholangitis: a comprehensive overview**. *Hepatol Int* 2017, **11**:485–499.
29. He JY, Ge WH, Chen Y: **Iron deposition and fat accumulation in dimethylnitrosamine-induced liver fibrosis in rat**. *World J Gastroenterol* 2007, **13**:2061–2065.
30. Tanimoto A, Yuasa Y, Shinmoto H, Jinzaki M, Imai Y, Okuda S, Kuribayashi S: **Superparamagnetic iron oxide-mediated hepatic signal intensity change in patients with and without cirrhosis: pulse sequence effects and Kupffer cell function**. *Radiology* 2002, **222**:661–666.
31. Choi Y, Huh J, Woo DC, Kim KW: **Use of gadoxetate disodium for functional MRI based on its unique molecular mechanism**. *Br J Radiol* 2016, **89**:20150666.

32. Fram EK, Herfkens RJ, Johnson GA, Glover GH, Karis JP, Shimakawa A, Perkins TG, Pelc NJ: **Rapid calculation of T1 using variable flip angle gradient refocused imaging.** Magn Reson Imaging 1987, **5**:201–208.
33. Kuribayashi H, Sekino M, Minowa T, Maitani Y, Ohsaki H, Tsushima S, Hirai S, Ueda M, Katayama Y: **Accuracy of equilibrium magnetization mapping in sliced two-dimensional spoiled gradient-recalled echo pulse sequence with variable flip angle.** J Magn Reson Imaging 2013, **38**:1245–1250.
34. Sun S, Zeng H, Robinson DB, Raoux S, Rice PM, Wang SX, Li G: **Monodisperse MFe₂O₄ (M = Fe, Co, Mn) nanoparticles.** J Am Chem Soc 2004, **126**:273–279.
35. Fickert P, Stoger U, Fuchsbichler A, Moustafa T, Marschall HU, Weiglein AH, Tsybrovskyy O, Jaeschke H, Zatloukal K, Denk H, Trauner M: **A new xenobiotic-induced mouse model of sclerosing cholangitis and biliary fibrosis.** Am J Pathol 2007, **171**:525–536.
36. Deoni SC, Rutt BK, Peters TM: **Rapid combined T1 and T2 mapping using gradient recalled acquisition in the steady state.** Magn Reson Med 2003, **49**:515–526.
37. Siedek F, Muehe AM, Theruvath AJ, Avedian R, Pribnow A, Spunt SL, Liang T, Farrell C, Daldrup-Link HE: **Comparison of ferumoxitol- and gadolinium chelate-enhanced MRI for assessment of sarcomas in children and adolescents.** Eur Radiol 2020, **30**:1790–1803.
38. Sheng RF, Wang HQ, Yang L, Jin KP, Xie YH, Fu CX, Zeng MS: **Assessment of liver fibrosis using T1 mapping on Gd-EOB-DTPA-enhanced magnetic resonance.** Dig Liver Dis 2017, **49**:789–795.
39. Koo TK, Li MY: **A Guideline of Selecting and Reporting Intraclass Correlation Coefficients for Reliability Research.** J Chiropr Med 2016, **15**:155–163.
40. Poynard T, Bedossa P, Opolon P: **Natural history of liver fibrosis progression in patients with chronic hepatitis C. The OBSVIRC, METAVIR, CLINIVIR, and DOSVIRC groups.** Lancet 1997, **349**:825–832.

Figures

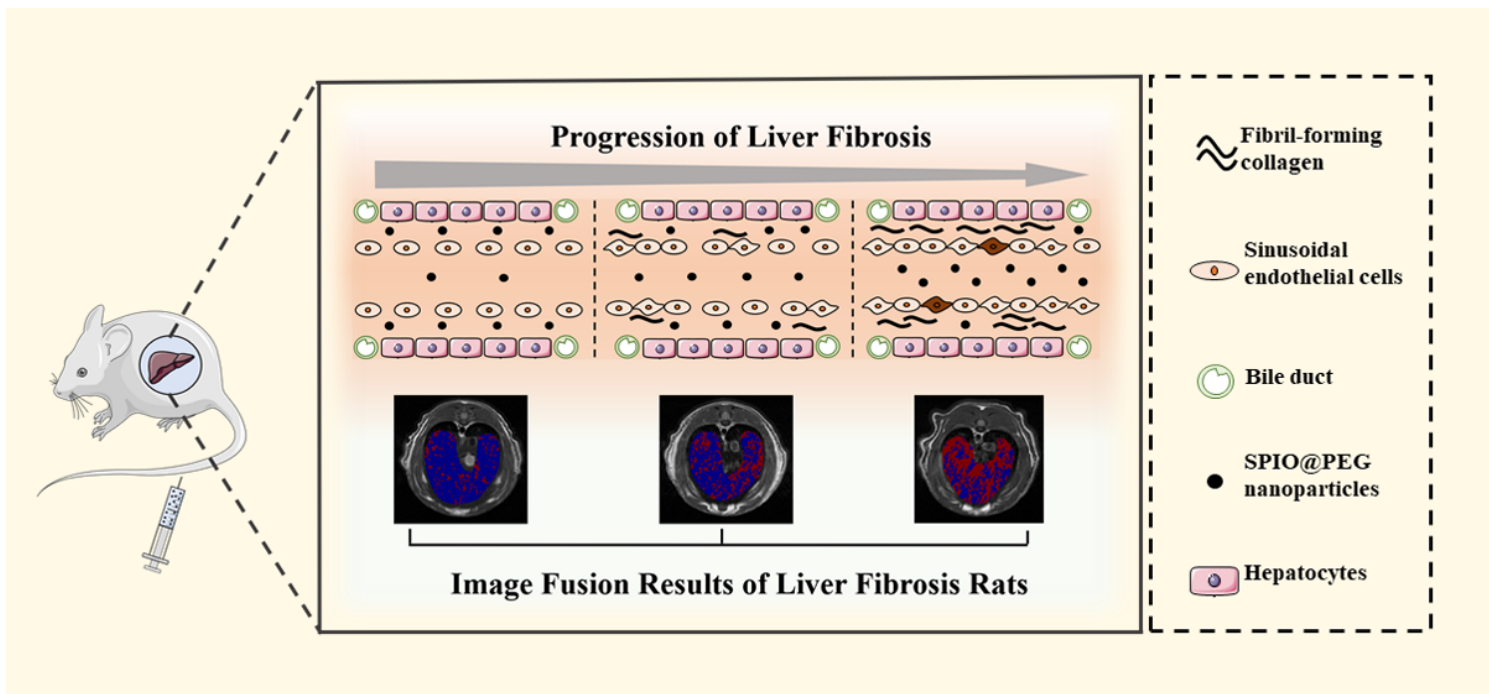


Figure 1

Illustration of the hepatic fibrosis induced iron nanoparticle distribution changes and the corresponding image fusion results at the progression of liver fibrosis.

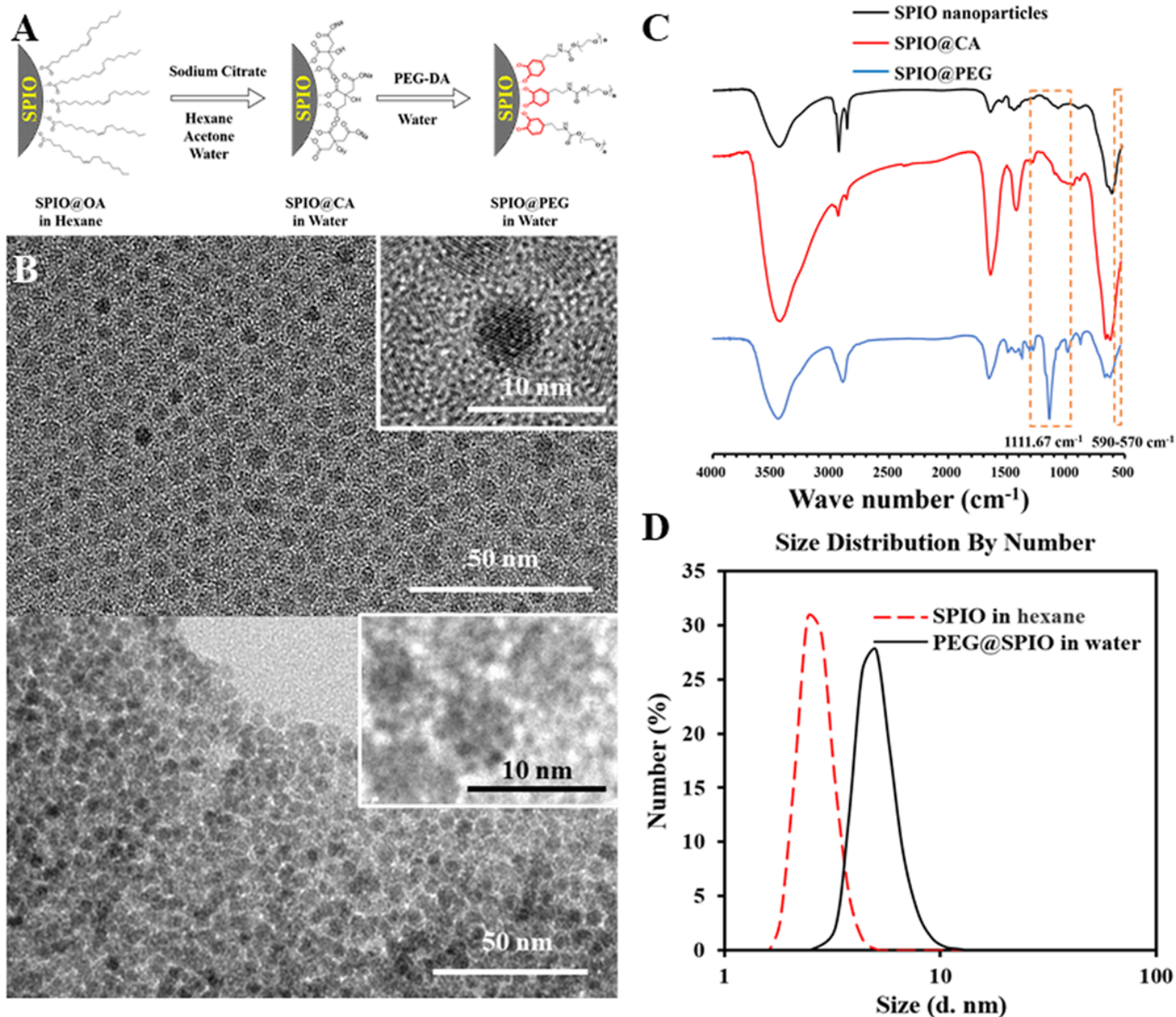


Figure 2

PEGylated Superparamagnetic Iron Oxide Nanocrystalline (SPIO@PEG). (A) The schematic preparation of SPIO@PEG. (B) Transmission electron microscopy (TEM) and HRTEM of hydrophobic SPIO (SPIO@OA) and hydrophilic SPIO (SPIO@PEG). (C) Fourier transform infrared (FTIR) spectra of SPIO@OA, SPIO@CA, and SPIO@PEG. (D) Dynamic light scattering (DLS) distribution of SPIO@OA (in hexane) and SPIO@PEG (in water).

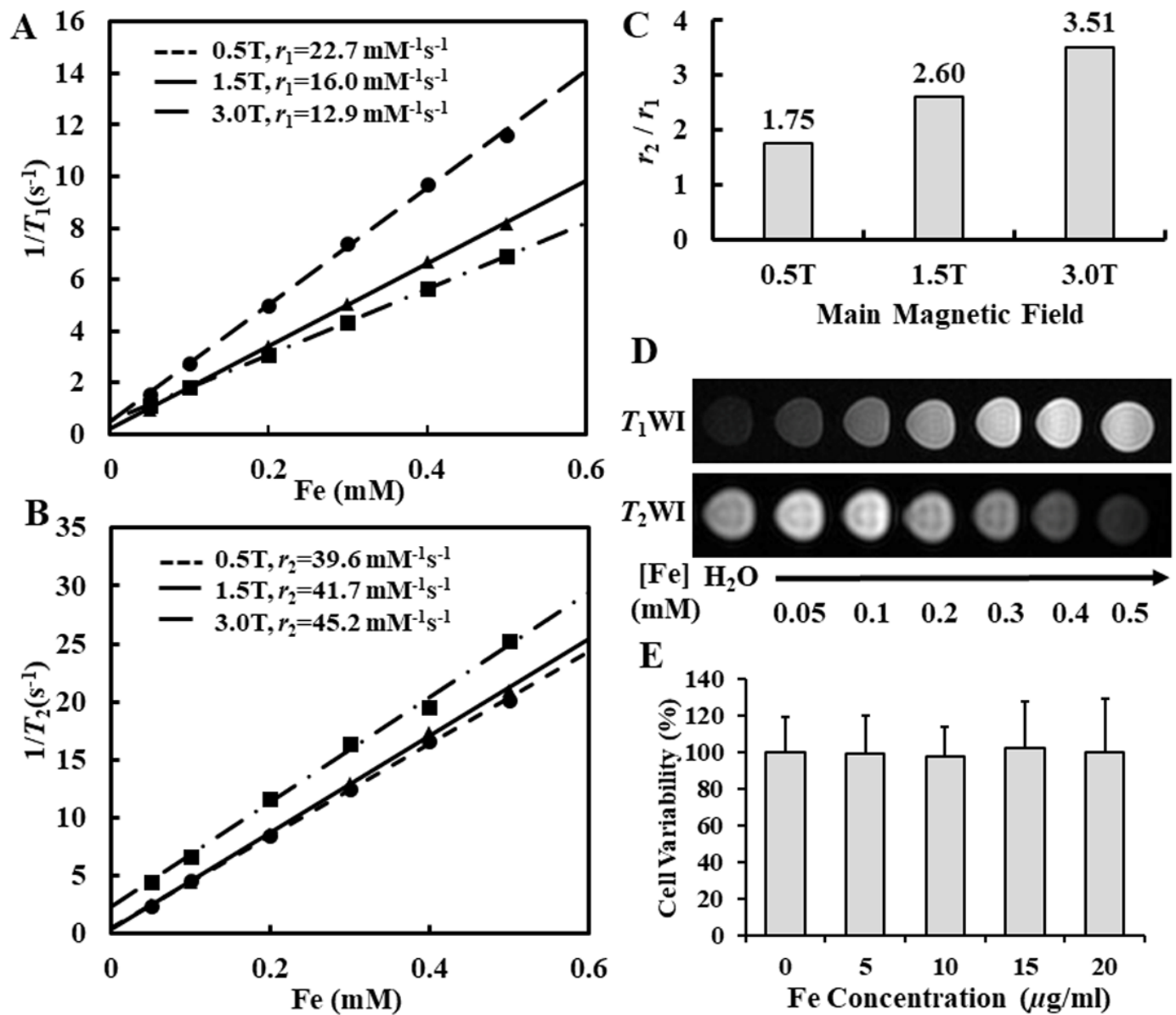


Figure 3

MRI Contrast enhancement study of PEGylated Superparamagnetic Iron Oxide Nanocrystalline (SPIO@PEG) in vitro. Longitudinal relaxation rate ($1/T_1$, s^{-1}) (A) and transverse relaxation rate ($1/T_2$, s^{-1}) (B) as a function of Fe concentration (mM) for SPIO@PEG at 0.5, 1.5, and 3.0 T. (C) r_2/r_1 rates of SPIO@PEG at 0.5, 1.5, and 3.0 T. (D) T_1 and T_2 -weighted MRI images of SPIO@PEG aqueous solution at clinical 3.0 T MR scanner (T_1 WI: spin-echo sequence, TR = 200 ms, TE = 9 ms, slice thickness = 3 mm, flip angle 90°; T_2 WI: spin-echo sequence, TR = 2500 ms, TE = 100 ms, slice thickness = 3 mm, flip angle 90°). (E): Cell cytotoxicity assay of SPIO@PEG incubated with Hep G2 cells for 24 h. Each data represents the mean \pm SD.



Figure 4

Masson and H&E staining of SD rat hepatic tissues. Liver specimens were extracted for pathological exams after 0, 1, 4, 8, and 12 weeks of DDC induction which representing biliary fibrosis stages of S0, S1, S2, S3 and S4, respectively.

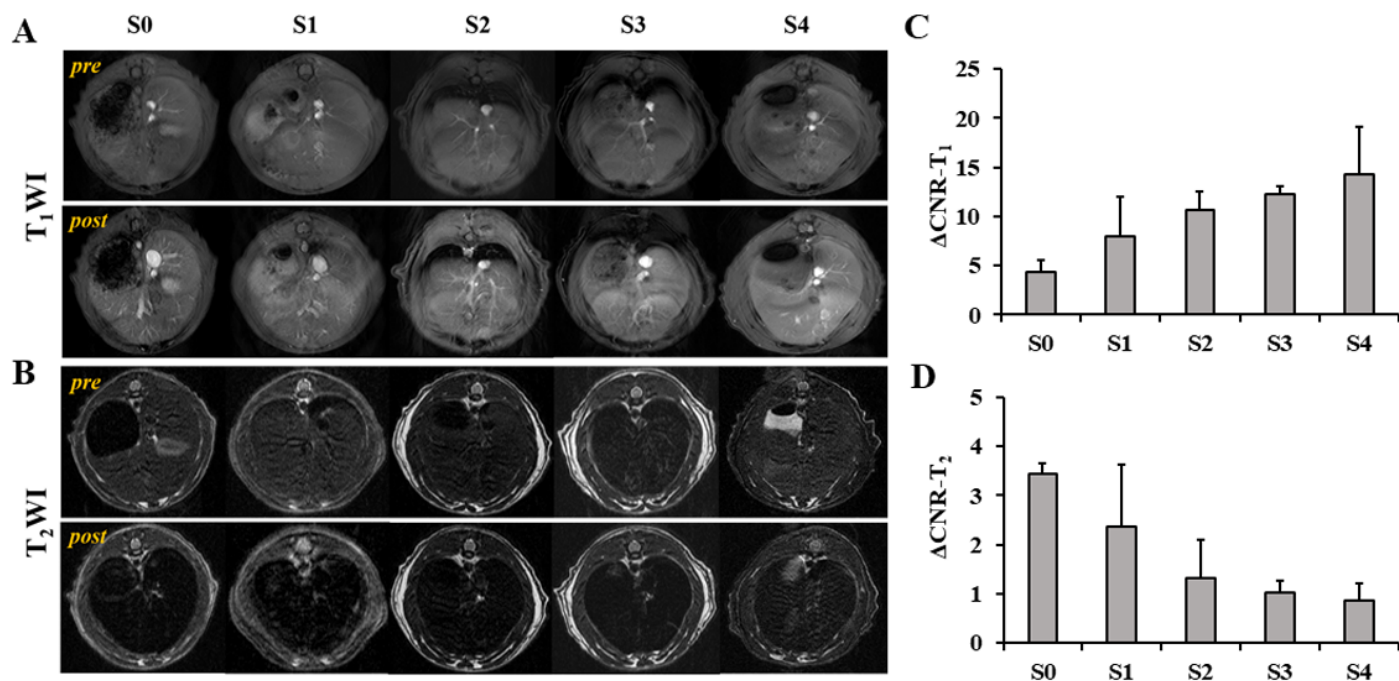


Figure 5

T_1 - T_2 dual-modal contrast enhancement study of liver fibrosis stage in rats. (A and B) Conventional T_1 and T_2 weighted images (T_1 WI and T_2 WI) of liver in different liver fibrosis stages pre and post intravenous injection of SPIO@PEG with a dose of 2.5 Fe mg/kg bodyweight. Quantitative measurements of the contrast-to-noise ratio (ΔCNR) of T_1 WI (C) and T_2 WI (D). All the groups were compared with each other by one-way analysis of variance (ANOVA). No significant differences were found among the different groups. T_1 WI: GRE sequence, TR = 9 ms, TE = 3 ms, FOV = 80 × 80 mm, slice thickness = 2 mm, flip angle 30°; T_2 WI: FSE sequence, TR = 4000 ms, TE = 76 ms, FOV = 80 × 80 mm, slice thickness = 2 mm, flip angle = 90°.

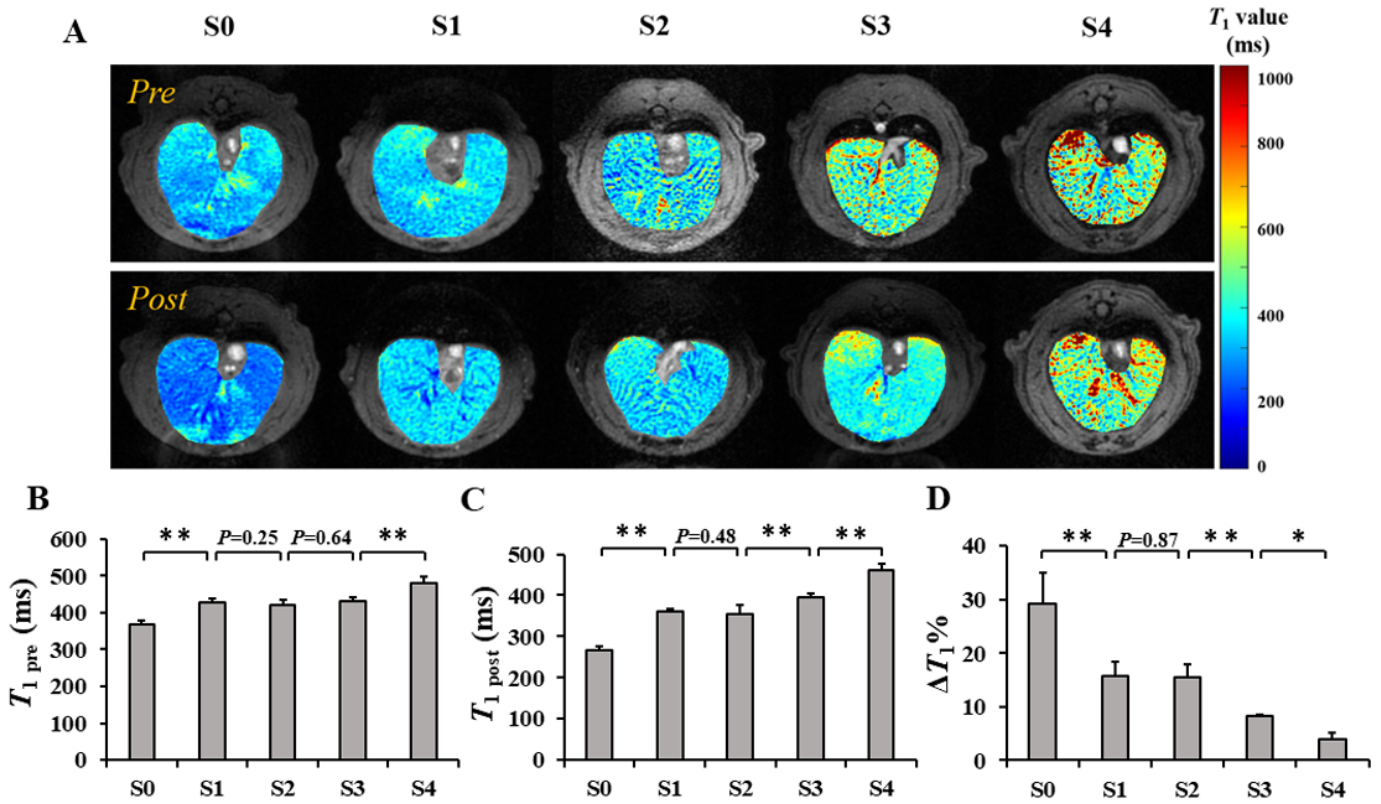


Figure 6

Quantitative analysis of hepatic T_1 values in different liver fibrosis stages pre and post administration of PEGylated superparamagnetic iron oxide (SPIO@PEG). (A) T_1 mapping images of liver pre and post intravenous injection of SPIO@PEG with a dose of 2.5 Fe mg/kg bodyweight. (B and C) Quantitative measurement of hepatic T_1 value in different liver fibrosis stages before ($T_{1\text{ pre}}$) and after ($T_{1\text{ post}}$) administration of SPIO@PEG, and the statistical differences of all the liver fibrosis stage groups were analyzed. (D) T_1 change rates ($\Delta T_1\%$) of different liver fibrosis stages and one-way ANOVA analysis results. *Refers to $P < 0.05$. **Refers to $P < 0.01$.

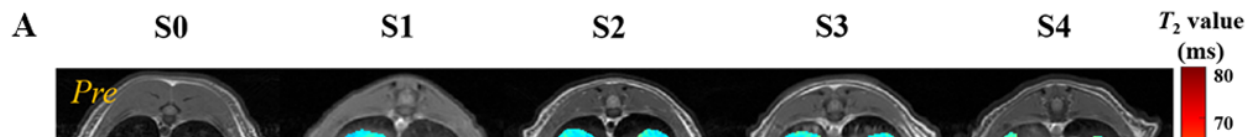


Figure 7

Quantitative analysis of hepatic T_2 values in different liver fibrosis stages pre and after post administration of PEGylated superparamagnetic iron oxide (SPIO@PEG). (A) T_2 mapping of liver pre and post intravenous injection of SPIO@PEG with a dose of 2.5 Fe mg/kg bodyweight. (B and C) Quantitative measurement of hepatic T_2 value in different liver fibrosis stages before ($T_{2\text{ pre}}$) and after ($T_{2\text{ post}}$) administration of SPIO@PEG, and the statistical differences of all the liver fibrosis stage groups were analyzed. (D) T_2 change rates ($\Delta T_2\%$) of different liver fibrosis stages and one-way ANOVA analysis results. *Refers to $P < 0.05$. **Refers to $P < 0.01$.

Image not available with this version

Figure 8

Image fusion results and illustration of the logic gate process. (A) The fused images of liver fibrosis in different stages after SPIO@PEG contrasted enhanced. (B) Illustration of the logic gate process. Both T_1

and T_2 values are higher than the threshold value can be outputted positive pixel. (a) Pixel of T_1 and T_2 mapping in either T_1 or T_2 but do not satisfy logic gate output with negative results (blue). (b) both the pixels in T_1 and T_2 mapping were higher than the threshold value and fulfill logic gate output with positive pixel (red). (C) Quantitative measurements of positive pixel ratio (PPR) different liver fibrosis stages before (pre) and after (post) administration of SPIO@PEG. *Refers to $P < 0.05$. **Refers to $P < 0.01$.

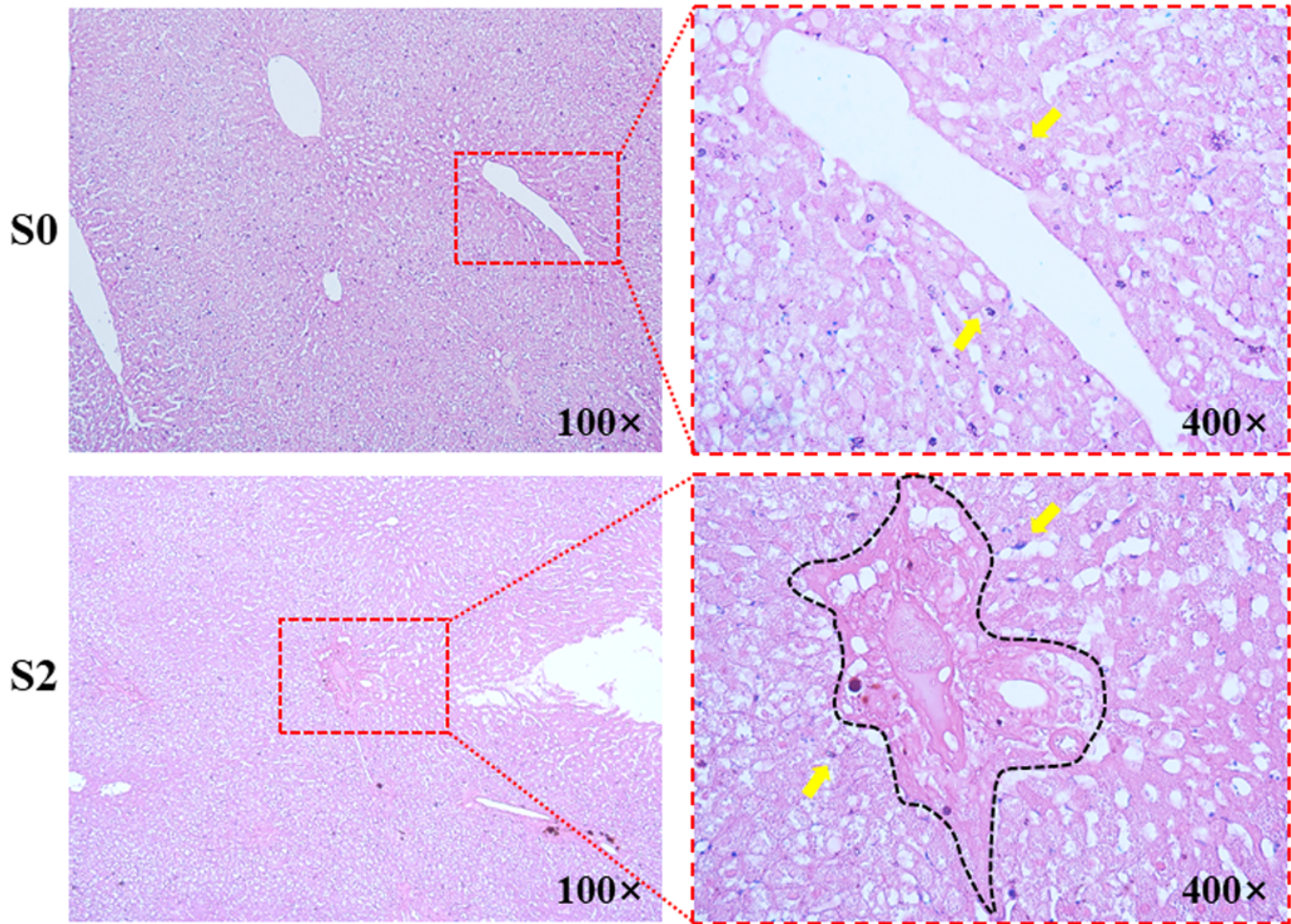


Figure 9

Prussian blue staining of SD rat hepatic tissue after administration of PEGylated superparamagnetic iron oxide (SPIO@PEG). In healthy group (S0), iron particles were randomly distributed in hepatic sinus (yellow arrowhead). In fibrotic groups (S2), iron particles only distribute along outer edge of fibrotic septa (yellow arrowhead).